Corrosion Science 253 (2025) 112990

Contents lists available at ScienceDirect

Corrosion Science

journal homepage: www.elsevier.com/locate/corsci

Exceptional high-temperature corrosion resistance of multi-component alloys via modulating Al and Nb

Hao Shi [a,b,*], Xukai Zhang [a], Chang Liu [a,c], Xing Gong [d], Yue Li [a], Raheleh Azmi [e,f], Yilun Gong [a], Dirk Ponge [a], Alfons Weisenburger [b,**], Georg Müller [b]

[a] Max Planck Institute for Sustainable Materials, Düsseldorf, Germany
[b] Institute for Pulsed Power and Microwave Technology (IHM), Karlsruhe Institute of Technology (KIT), Hermann, von-Helmholtz-Platz 1, 76344 Eggenstein-Leopoldshafen, Germany
[c] Center for Alloy Innovation and Design (CAID), State Key Laboratory for Mechanical Behavior of Materials, Xi'an Jiaotong University, Xi'an 710049, China
[d] Advanced Nuclear Energy Research Team, Department of Nuclear Science and Technology, College of Physics and Optoelectronic Engineering, Shenzhen University, Shenzhen 518060, China
[e] Institute for Applied Materials (IAM), Karlsruhe Institute of Technology (KIT), Hermann, von-Helmholtz-Platz 1, 76344 Eggenstein-Leopoldshafen, Germany
[f] Department of Chemistry-Ångström Laboratory, Structural Chemistry, Uppsala University (UU), Lägerhyddsvägen 1, Uppsala 75121, Sweden

ARTICLE INFO

Keywords:
AlCrFeNi
Multi-component alloy (MCA)
Liquid metal corrosion
Alumina scale formation
Chemical compatibility

ABSTRACT

The chemical compatibility of metallic materials with thermal transfer/storage media, which often involves aggressive working conditions (i.e., high-temperature, corrosive environments), challenges the safe operations of advanced and sustainable energy-related infrastructures. Here, we report the corrosion-oxidation behaviors of three multi-component alloys (MCAs) when exposed to a corrosive heavy-liquid metal condition (*i.e.*, molten Pb at 650 °C with 10^{-6} wt% oxygen dissolved). The two compositions, $Al_{0.36}Cr_{0.67}FeNi_{0.98}$ (HAl11) and $Al_{0.27}Cr_{0.71}FeNi_{1.16}Nb_{0.17}$ ($HAl8^{Nb}$), show excellent corrosion-resistance via passivating a protective oxide scale on the alloy surface. Further characterizations of the oxide layers differentiate their corrosion-oxidation mechanisms: a protective Al_2O_3 oxide layer (with Cr and Fe segregation outmost) formed on HAl11 and a duplex oxide layer (outward growth of $FeCr_2O_4/Cr_2O_3$ layer plus inward growth of an Al_2O_3 layer) with internal oxidation on $HAl8^{Nb}$. Adding Nb improved the corrosion-oxidation resistance ("Nb-doping effect") by enhancing the outward diffusion of metallic elements and promoting the rapid establishment of an alumina scale. Besides, the presence of $AlNbO_4$, which was predicted by thermodynamics calculation, lying between the spinel and Al_2O_3 formation, was also confirmed by experimental observations. Our findings advance the mechanistic understanding of MCAs' performances in extreme conditions and provide novel strategies for designing corrosion-resistant alloys targeting aggressive application environments.

1. Introduction

In the context of a global increase in energy consumption, while simultaneously considering the decarbonization goals [1], there is a growing focus on developing and deploying sustainable and large-scale energy production and storage systems. These include concentrated solar power (CSP) towers [2,3], liquid metal batteries (LMBs) [4,5], methane cracking for hydrogen production [6,7], and fission and fusion reactors [8–10]. Such systems are often associated with high temperatures, mechanical loads, and/or radiation effects, which place significant demands on the materials used. Alternative thermal energy transfer or storage media, namely liquid metals (*i.e.*, Pb, Na, Sn, Pb-Bi eutectic (LBE), Pb-Li alloy) [4,5,11,12], molten salts [13,14], and supercritical CO_2 [15], are considered for such applications because of their excellent thermo-physical properties, abundant source and in the case of liquid metals their wide liquid temperature range which allows almost pressure-less operation. For instance, the thermal conductivity of LBE is 260 and 195 times the value of air and steam at 600 °C, respectively [16], making them (Pb or PbBi eutectic (LBE)) ideal cooling/heat transfer media for systems working at elevated temperatures.

However, the aggressive characteristics of liquid metals, namely liquid metal corrosion (LMC) [16] and liquid metal embrittlement (LME,

* Corresponding authors at: Max Planck Institute for Sustainable Materials, Düsseldorf, Germany.
** Corresponding author.
E-mail addresses: shisjtu@outlook.com (H. Shi), alfons.weisenburger@kit.edu (A. Weisenburger).

https://doi.org/10.1016/j.corsci.2025.112990
Received 10 January 2025; Received in revised form 15 April 2025; Accepted 28 April 2025
Available online 28 April 2025

mainly occurring in ferritic/martensitic steels at 350–400 ℃ [17]), cause severe property degradation of conventional structural-metallic materials, limiting the systems' operation temperature. In particular, the corrosion of metallic materials in molten Pb/LBE is mainly driven by the dissolution of alloying elements like Ni, Mn, Cr, and Fe [16]. Selective leaching of austenite stabilizers like Ni or Mn can lead to ferritization of the austenite phase in the corroded zone [18]. Moreover, the corrosion process is intensified as the operation temperature increases due to the enhanced solubility of elements in liquid metal at increasing temperatures [19,20]. Introducing oxygen into the melts combined with strong oxide-forming constituents, being able to in-situ passivate an oxide film on the alloy surface, is a highly desirable corrosion mitigation strategy [21]. Moreover, alloying elements like Al, Si, and Cr, which can form a dense and protective oxide layer with a low oxidation rate (*i.e.*, $K_p(Al_2O_3)= 10^{-7}\sim10^{-8}$ $mg^2{\cdot}cm^{-4}{\cdot}s^{-1}$ (900 ℃) [22]), were added in steels for further improving their corrosion-oxidation resistance for such applications [23,24]. A previous study of two Al-alloyed/alumina-forming austenitic (AFA) alloys (Fe-(15−16) Cr-4Al-(24, 28)Ni, wt%) exposed to molten Pb showed their good corrosion resistance up to 600 ℃ [20]. However, the corrosion attack intensified as the tested temperature increased to 650 ℃ due to the enhanced Ni solubility in liquid Pb [20,25]. Therefore, the current work aims to search for new alloy design strategies to improve the materials' corrosion resistance at or above 650 ℃ with a low oxidation rate.

In the last two decades, a new alloy family, called high entropy alloy (HEA) or multi-component alloy (MCA), has received wide attention due to its intriguing compositions, microstructures, and engineering properties [26,27]. This type of alloy is particularly suited for applications in extreme environments, as its composition and microstructure can be tailored to suit specific requirements. The high thermal stability and irradiation resistance of WTaCrVHf [28], the unique thermomechanical properties of the oxide layer grown on $AlCrTiVNi_5$ [29], the strong and ductile high-temperature soft magnet $Fe_{35}Co_{30}Ni_{30}Ta_5$ [30], and other ultra-strong and ductile MCAs (via precipitates or interfaces hardening) like $Al_{0.5}Cr_{0.9}FeNi_{2.5}V_{0.2}$ [31], $Al_9(CoCrFeMnNi)_{91}$ [32], $Ni_{43.9}Co_{22.4}Fe_{8.8}Al_{10.7}Ti_{11.7}B_{2.5}$ [33] are noteworthy. By screening the periodic table of elements and considering the role of alloying elements on the properties of steel [34], a four-element-based MCA system Al-Cr-Fe-Ni was finally selected [35,36], in which Ni helps stabilize the FCC phase (face-centered cubic, avoiding LME), Al promotes the formation of an Al_2O_3 scale, and Cr improves the corrosion/mechanical properties and reduces the critical amount of Al needed via the "third-element effect [37]".

In an oxygen-containing heavy liquid metal environment, the competition between dissolution corrosion and oxidation processes determines whether a metal/steel can form a protective oxide layer during the service. The oxide scale growth rate can be quantified by Tedmon's model [38]: $\frac{d\delta}{dt}=k_p\text{-}Q_c$, where δ is the thickness of the oxide film, k_p is the oxidation rate, and Q_c is the corrosion rate. Finding a way to increase the value of k_p and/or decrease the magnitude of Q_c can promote the formation of a protective oxide scale in such a condition. Besides, Wagner's oxidation model [39] defines the criteria for the transition from internal to external (protective) oxidation in an A-B alloy system, the critical amount of solute B can be evaluated by Eq. (1):

$$N_B^0 > \left(\frac{\pi g^*}{2b}\frac{N_O^S D_O V_m}{D_B V_{OX}}\right)^{1/2} \tag{1}$$

where, g^* is the critical volume fraction of internal oxide beyond which an external scale may form (it is usually set to 0.3 [40]), b is the stoichiometric coefficient for the oxide, N_O^S is oxygen solubility in the alloy, D_O is the oxygen diffusion coefficient in the alloy, D_B is the diffusion coefficient of B in the alloy, and V_m and V_{OX} are molar volumes of bulk alloy and oxide respectively.

This equation governs the design strategy for the most high-temperature oxidation/corrosion alloys, *i.e.*, simply increasing Al to a critical value N_{Al}^0 to promote the formation of an external Al_2O_3 scale. However, excessive Al addition results in ferritization of the bulk alloy since Al is a strong ferritic phase stabilizer. Besides, Wagner-Häuffe's rule [41] suggests that doping high-valence ions into oxides with low-valence cations accelerates the diffusion of ions within the oxides. Our calculations also indicate that adding Nb can enhance the bulk diffusion of alloying elements, which helps build an oxide scale rapidly. On the other hand, adding Nb to AFA steels and Ni-based superalloys was reported to improve their high-temperature mechanical properties, especially the creep resistance due to the formation of strengthening phases like Laves and $NbNi_3$ [34,42,43]. In this study, Nb was added to the Al-Cr-Fe-Ni system to reduce the value of N_{Al}^0, as a further strategy to modify its high-temperature properties (*i.e.*, corrosion and mechanical properties) without maintaining a high Al content.

In this work, the corrosion performances of three MCAs were investigated when exposed to molten Pb. The exposure results reveal that the surface degradation of the low Al-alloyed sample (7.9 at% Al) can be overcome either by increasing the Al concentration to 11.4 at%, or adding additional Nb (5.2 at%) while maintaining the same level of Al content. Further characterizations reveal the microstructure of the passivated oxide scale on the protected alloys and address their corrosion-oxidation mechanisms. Coupling experiments with the calculated results, we confirm the presence of Nb-Al-rich oxides in the oxide layer of the Nb-alloyed sample, giving a clue that adding Nb promotes the formation of a protective oxide scale in a lower Al concentration condition (8.7 at% *vs* 11.4 at%).

2. Materials and methods

2.1. Material and processing

Table 1 summarizes the chemical compositions of the three candidate alloys. The alloys, HAl8 and HAl11, were prepared based on Al-Cr-Fe-Ni with varying Al content. Here, "HAl" derives from "High entropy" and "Aluminum", and the number represents the nominal Al concentration. The third alloy, $HAl8^{Nb}$, is based on Al-Cr-Fe-Ni-Nb, and the Al content was maintained at the same level as the HAl8. All samples were prepared by arc melting the mixture of pure elements (purity> 99.99 wt %) in a water-chilled copper mold. During the sample's preparation, the ingot was flipped over and re-melted at least five times to facilitate the composition homogenization. The chemical compositions of the prepared samples were measured by ICP-OES (mode: Thermo ICAP PRO) with a working power of 1150 W, plasma gas flow rate of 15 L/min, auxiliary gas flow rate of 0.5 L/min, nebulizer gas flow rate of 0.5 L/min and cooling gas flow rate of 12.5 L/min. The weight percentage (wt%) was obtained by the following Eqs. (2) and (3).

$$Cx(mg/kg) = \frac{Co(mg/L)*f*Vo(mL)*10^{-3}}{m(g)*10^{-3}} = \frac{C1(mg/L)*Vo(mL)*10^{-3}}{m(g)*10^{-3}} \tag{2}$$

$$wt.\% = \frac{Cx(mg/kg)}{10^6}*100\% \tag{3}$$

Where C_x is the obtained element concentration, C_o is the element concentration in the solution, f is the dilution-multiple, V_o is the volume of the dissolved solution, C_1 is the element concentration in the original dissolved solution (before dilution), m is the mass of the analyzed sample.

2.2. Corrosion tests

The corrosion test was performed in a stagnant molten Pb pool with controlled oxygen concentration (10^{-6} wt%) in the COSTA facility (**CO**rrosion test stand for **ST**agnant liquid **A**lloys). The exposure

Table 1
Nominal composition of candidate alloys and their mole formulas and the chemical compositions of bulk materials measured by ICP-OES with error < 0.1 wt%.

Code	Nominal composition (at%)	Mole formula	Al (at%)	Cr (at%)	Fe (at%)	Ni (at%)	Nb (at%)
HAl8	$Al_{8.0}Cr_{23.2}Fe_{34.0}Ni_{34.8}$	$Al_{0.23}Cr_{0.68}FeNi_{1.02}$	7.9	21.0	35.0	36.1	–
HAl11	$Al_{11.7}Cr_{22.4}Fe_{33.3}Ni_{32.6}$	$Al_{0.36}Cr_{0.67}FeNi_{0.98}$	11.4	21.8	33.5	33.3	–
$HAl8^{Nb}$	$Al_{8.2}Cr_{21.4}Fe_{30.3}Ni_{35.0}Nb_{5.1}$	$Al_{0.27}Cr_{0.71}FeNi_{1.16}Nb_{0.17}$	8.7	20.2	30.3	35.6	5.2

temperature was 650 ℃ with a duration of 3500 h. The dimensions of the samples used for the experiment are 10 mm in diameter and 1.5 mm in thickness. Before the exposure, all samples were grounded to a 1200 grit surface finish. All the samples were cleaned with distilled water, acetone, and ethanol in an ultrasonic bath and dried before the corrosion tests. After the corrosion exposure, samples were extracted from liquid Pb, and the remaining adherent Pb was cleaned by immersing the samples into a solution of ethanol, acetic acid, and hydrogen peroxide (1:1:1) for 15 min. The uniaxial tensile tests were performed in the air by the tensile machine "LABET-1" [44] with a strain rate of 5×10^{-5} s^{-1} at 350 and 500 ℃, respectively. The samples were manufactured into a cylindrical shape with the geometrical dimensions shown elsewhere [44].

2.3. Microstructure characterization

The microstructures of the investigated materials were characterized by a ZEISS Sigma scanning electron microscope (SEM, model: Zeiss LEO 1530 VP), equipped with electron dispersive X-ray spectroscopy (EDS). The accelerating voltage of the SEM was 20 keV with a working distance of 8 mm. The electron backscatter diffraction analysis (EBSD, Zeiss-Crossbeam XB 1540 focused ion beam-SEM instrument) was also conducted to characterize the bulk material operated in 15 kV, 7.4 nA with a step size of 0.05 μm. The data analysis was performed using the TSL OIM software package. In addition, a grazing incidence X-ray diffraction (GIXRD, detector: HyPix 3000 (2D detector)) was also applied to investigate the types of oxides formed on the sample surface. The incident angle is 2° with a scan rate of 0.75 °/min. The Cu Kα line (λ=0.15409 nm, 45 kV, and 200 mA) was used as a source for diffraction. Regarding the cross-sectional analysis, a Ni-layer (~25 μm) was electroplated on the sample surface to prevent damage of the surface oxide layer during the polishing process.

The surface oxide film was also characterized by X-ray photoelectron spectroscopy (XPS, K-Alpha+ instrument from Thermo Fisher Scientific) with a monochromatic Al-Kα X-ray source (1486.6 eV) and X-ray spot size of 400 μm. The 8 eV electrons and low-energy Ar ions were applied by a K-Alpha+ charge compensation system to reach the charge neutralization state. The Thermo Advantage software was also employed to acquire and process the raw data. The obtained spectra were further deconvoluted into one or more Voigt profiles [45]. The C 1 s peak of adventitious hydrocarbons with binding energy (BE) of 285.0 eV was used as a reference. For the quantification process, three parameters, namely scofield sensitivity factors [46], analyzer transmission function, and the effective attenuation lengths (EALs), were considered. EALs were calculated according to the standard TPP-2 M formalism [47]. In addition, the depth profile was also obtained by sputtering the sample surface with monoatomic Ar ions working in 4 keV energy and a low current.

Transmission electron microscopy (TEM) lamella was prepared by a FEI Helios 600 crossbeam focused ion beam (FIB) at 30 kV down to an ion current of approximately 24 pA. Scanning transmission electron microscopy (STEM) was performed on FIB specimens at 300 kV with a probe-corrected Titan Themis 60–300 (Thermo Fisher Scientific), which is equipped with four synchronized EDS detectors (ChemiSTEM system). For STEM imaging and EDS elemental mapping, a semi-convergence angle of 23.8 mrad and semi-collection angles of the high-angle annular dark-field (HAADF) detector of 73 and 200 mrad were selected for the characterization.

2.4. Thermodynamic calculation

Thermodynamic calculations were performed using Thermo-Calc 2024a, coupled with TCNI8/TCOX10 thermodynamic database and MOBNI3 mobility database. Major phases, including FCC_A1, FCC_$L1_2$, BCC_A2, CORUNDUM, SPINEL, HALITE, $ALNB_{11}O_{29}$, COLUMBITE, MGWO4_TYPE and $CRNB_2O_4$, were considered in the calculations.

3. Results

3.1. Corrosion performance evaluation

Three MCAs, HAl8, HAl11, and $HAl8^{Nb}$, were selected for the investigation (see 2.Materials and methods section for the detailed compositions). The two alloys HAl8 and HAl11 are based on the nominal compositions $Fe_{(33-34)}$-$Cr_{(22-23)}$-$Ni_{(32-35)}$-Al_x (x = 8.0 at% for HAl8 and 11.7 at% for HAl11). Another alloy $HAl8^{Nb}$ is derived from HAl8's composition (same level Al but reduced Fe content) and adding Nb additionally (5.1 at%). The bulk microstructures of the three as-prepared samples were characterized by SEM and EBSD (Supplementary Fig. S1). HAl8 forms a single FCC (face-centered cubic) solid solution, while the other two alloys form FCC plus B2 (NiAl) phases (HAl11) or FCC plus Laves (Fe_2Nb) phases ($HAl8^{Nb}$).

Fig. 1a presents the surface morphologies of all three samples after the corrosion exposure. Sample HAl8 shows multiple evidence of material degradations, including pores, microcracks, and loss of Cr and Fe in these regions (Supplementary Figs. (S2, S3)). Besides, small particles grown on the exposed surface are confirmed to be B2-NiAl phase (Supplementary Figs. (S2, S4) and Table S1). No protective oxide layer was detected according to the XPS characterization (Supplementary Fig. S5). Noting that the other two alloys with higher Al content (8.9 at% Al (HAl9) and 9.8 at% Al (HAl10)) were also prepared and exposed to the same conditions, and corrosion attacks in terms of oxide scale spallation or Pb penetration were observed (Supplementary Table S2 and Fig. S6). In comparison, both the surfaces of HAl11 and $HAl8^{Nb}$ are entirely covered by a passivating oxide layer without evidence of material loss or oxide scale exfoliation. Besides, oxide nodules (HAl11) and ripple-shaped surface morphology ($HAl8^{Nb}$) were also observed. To identify the surface oxides, GIXRD measurement was employed (X-ray penetration depth < 1 μm [48]), and according to the spectra, oxide phases including Cr_2O_3 (space group $R\bar{3}c$) and Fe_3O_4 (space group $Fd\bar{3}m$) were identified in both samples, shown in Fig. 1b. The Fe_3O_4 phase in HAl11 is attributed to the observed oxide nodules (Fig. 1a). Besides, metallic phases like FCC and B2-NiAl are also marked in HAl11. The main phases obtained from bulk $HAl8^{Nb}$ are FCC, B2-NiAl, and $NbNi_3$.

The SEM cross-sectional images of both materials are shown in Fig. 1c. A Ni-coating layer was deposited to prevent damage to the surface oxide scale from sample polishing. Both samples' surfaces are covered by a dense oxide layer. Below the surface scale of HAl11 (c-1, c-3), a transitional layer (TL), featured with Cr-rich precipitates and depleted in B2 phase (from bulk alloy), forms due to oxidation-induced elements inter-diffusion [20]. According to the cross-sectional image of $HAl8^{Nb}$ (c-2), the entire bulk material, including the Laves phase region, is covered by an oxide layer. Its thickness is not as uniform as that of HAl11. Besides, a few bright contrast regions beneath the oxide scale (see the magnified image in c-4), differing from the Laves phase in size and chemical composition, were confirmed to be $NbNi_3$ according to

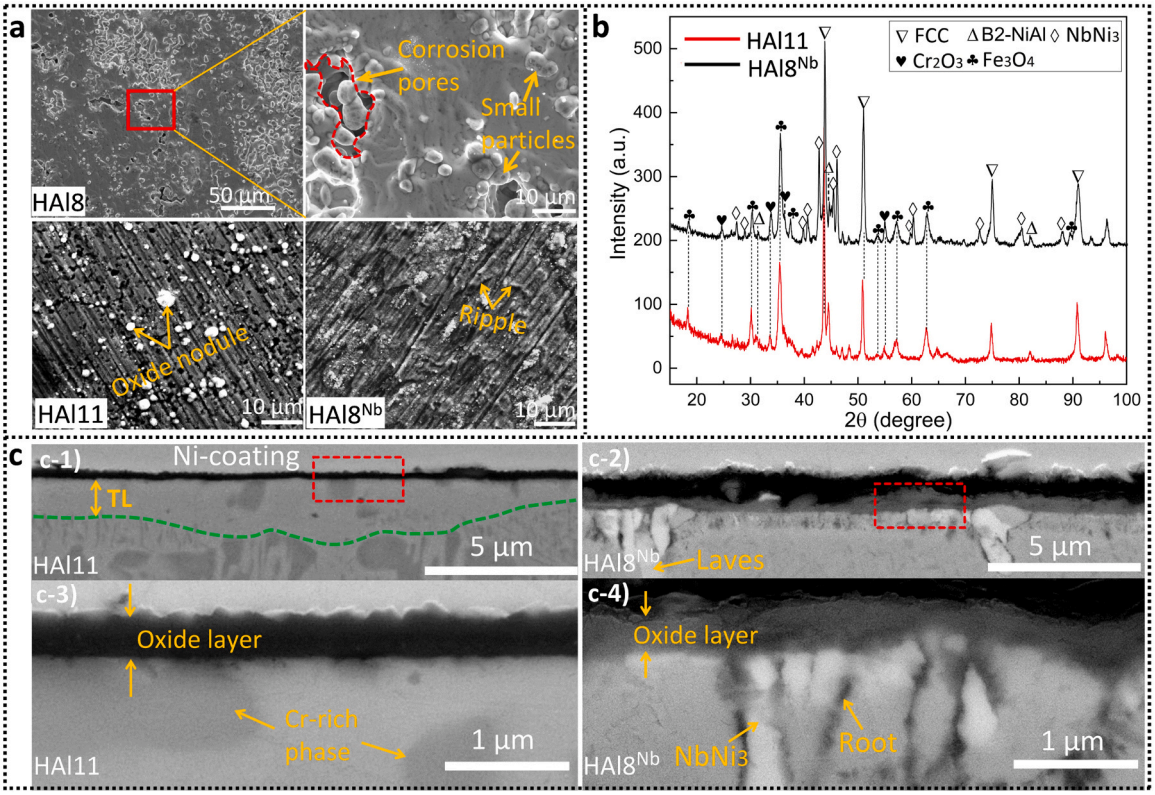

Fig. 1. (a) Surface morphology of HAl8 (including the magnified image of the red frame region), HAl11 and HAl8^{Nb} after 3500 h exposure in molten Pb at 650 °C; (b) GIXRD spectra of HAl11 and HAl8^{Nb} after corrosion test; (c: c-1, c-2) SEM cross-sectional images of the oxide layer formed in HAl11 and HAl8^{Nb}, (c-3) is the enlarged image of the red rectangle region in (c-1), (c-4) is the enlarged image of the red rectangle region in (c-2).

GIXRD (Fig. 1b) and EDS analysis (Supplementary Fig. S7). Additionally, some roots with dark contrast, adjacent to the bright phases, penetrate inside the alloy matrix. However, the phase/composition is unable to be identified by GIXRD or SEM-EDS analysis, which needs further characterization by TEM.

3.2. Corrosion-oxidation behavior of HAl11

XPS characterization was employed to analyze the chemical composition of the surface scale in HAl11, as shown in Fig. 2. The Al 2 s peak with a binding energy (BE) of 118.9 eV is identified, which is assigned to Al^{3+} [49]. The Cr 2p spectrum shows multiplet, and all sub-peaks belong to Cr^{3+}, confirming the formation of Cr_2O_3. The Fe 2p spectrum also has multiplet, consisting of six sub-peaks. Two located at the lower BE positions (< 710 eV) originate from Fe^{2+}, while the rest with a higher BE (> 710 eV) are from Fe^{3+}. Unlike HAl8 (Supplementary Fig. S5), no metallic Fe was detected. The deconvolution of the O 1 s spectrum creates three sub-peaks with the BEs of 533.0, 531.6, and

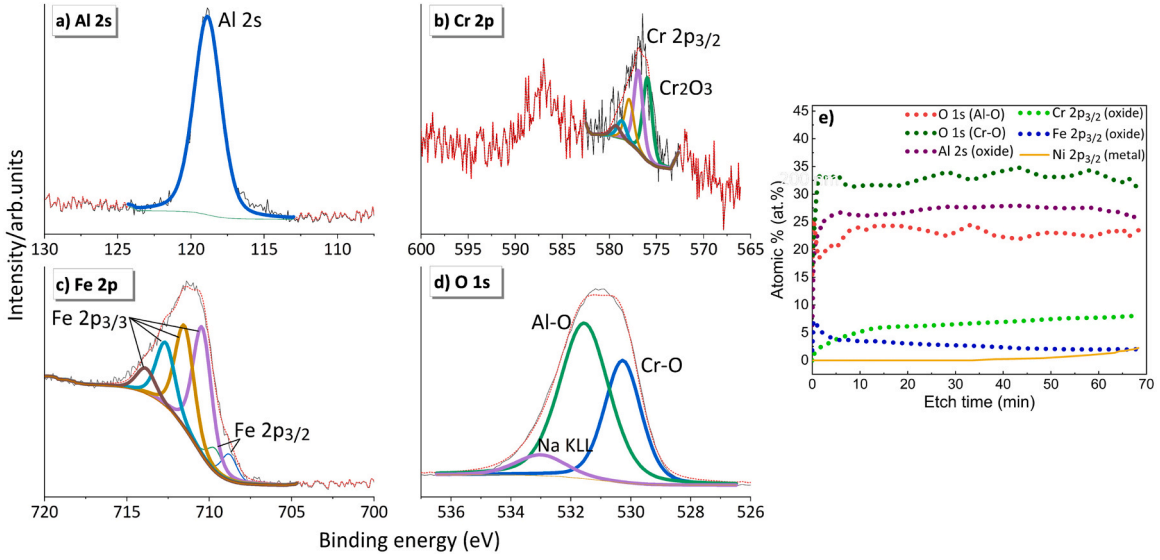

Fig. 2. XPS surface spectra obtained from HAl11 after corrosion exposure, (a) Al 2 s, (b) Cr 2p, (c) Fe 2p, (d) O 1 s, (e) Depth profile of elements concentration evolution as a function of sputter time (from 0 to 70 mins).

530.3 eV, which belong to Na KLL (impurity in Pb), Al-O, and Cr-O, respectively. Moreover, the sputtering process was also conducted to unveil the composition evolution in the oxide layer (Fig. 2e). The detected O signal is mainly from Al-O and Cr-O oxides. According to the measurement, the O content from Al-O fluctuates at around 32 at%, while an average value of O from Cr-O is around 23 at%. This is also stressed by the detected oxidized states of alloying elements, where Al accounts for over 25 at%. Other elements like Cr and Fe were also detected. The Cr concentration increases gradually and stabilizes at a value around 7 at%, while the Fe behaves oppositely and finally stabilizes at around 2 at%. No Ni signal was detected through the whole thickness direction, which is an essential hint of the protectivity of the oxide layer.

Fig. 3a shows the TEM bright-field (BF) images and the selected area electron diffraction (SAED) obtained from the oxide layer region (Figs. 3a-1). A uniform oxide layer with a thickness of around 100 nm is observed above the alloy surface. No internal oxidation is visible. Besides, the ring patterns unravel the formation of poly-crystalline oxides. Despite the detected Cr_2O_3, the formation of corundum Al_2O_3 (space group $R\bar{3}c$) was also confirmed by the SAED. Further scanning TEM EDS mapping (Figs. 3a-2) and line scan (Fig. 3b) depicts the distribution of elements in the oxide scale, namely O and Al distributing in the whole oxide layer region. At the same time, Cr and Fe are locally enriched close to the surface region (less than 1/3 of the thickness). Moreover, EDS regional analysis (Area 1) was performed and depicted in Fig. 3b. According to the measurement, aluminum accounts for the majority of the detected alloying elements, with around 0.94 in the whole amounts of Al and Cr. Since corundum Al_2O_3 can form a complete solid solution with Cr_2O_3 [50], a formula corresponding to the Al_2O_3-Cr_2O_3 solid solution is provided, namely, $(Al_{0.94}Cr_{0.06})_2O_3$.

3.3. Corrosion-oxidation behavior of HAl8^{Nb}

Fig. 4 plots the XPS surface spectrum of HAl8^{Nb}. Like the HAl11, the signals obtained from Al 2 s, Cr 2p, and Fe 2p are from the oxidized state. The O 1 s profile is analogous to that obtained from HAl11. However, the relative ratio of Al-O to Cr-O differs from that of the HAl11. Besides, two peaks of Nb $3d_{3/2}$ and $3d_{5/2}$ were also detected, which were assigned to the oxidized Nb [51]. Further analysis via depth profile is shown in Fig. 4d. In the first 20 mins of sputtering, the concentration of O 1 s (Cr-O) is much stronger than that of O 1 s (Al-O). This trend changes after 20 mins of etching due to the decrease of O 1 s (Cr-O) and the increase of O 1 s (Al-O) concentrations. It is also revealed by the evolution of Al (oxide) and Cr (oxide) concentrations in the curve, which might indicate the change in the oxide layer structure. The weak Fe signal (oxide) detected at the beginning of the sputtering (< 10 mins) revealed the formation of the mixed Fe- and Cr- rich oxides. Though Nb (oxide) was also detected from the surface profile, the depth profile measurement indicated its relatively low content throughout the oxide layer, which required further investigation by high-resolution STEM.

Fig. 5 shows the TEM BF images and the SAEDs obtained from the oxide layer region. The alloy surface is covered by a non-uniform oxide layer. The thin part (left side of the oxide layer) corresponds to the Laves/$NbNi_3$ phase underneath, while the thick region (right side) is attached to the FCC phase region. For all surface regions, a duplex oxide layer structure is revealed, corresponding to an outward- and an inward-grown layer. The interface of the two layers is precisely located at the original metal surface. Besides, the dark contrast roots (observed in Figs. 1c-4) are internal oxidation (IO) roots that grow along the interface of the FCC and the Nb-rich phases (*i.e.*, Laves or $NbNi_3$). The thickness of the whole oxidized region (including the IO zone) varies from 200 nm to 900 nm. The SAEDs obtained from the oxide layer region show ring-shape patterns, confirming the formation of nano-crystal grains. The patterns obtained from the thin oxide layer region (Figs. 5b-1) are indexed as corundum Al_2O_3, as shown in Figs. 5b-2. Another SAED done on the thick part (Figs. 5c-1), where both the outer and the inner layers become thick, confirms the mixed signals from corundum Al_2O_3, Cr_2O_3, and $FeCr_2O_4$ as shown in Figs. 5c-2.

The chemical compositions of the oxide layer were further analyzed by STEM-EDS mapping, shown in Fig. 6a. The outer layer mainly consists of O, Cr, and Fe signals. In contrast, the inner layer is mainly enriched in O, Al, Cr, and Al accounts for the majority. The local Cr

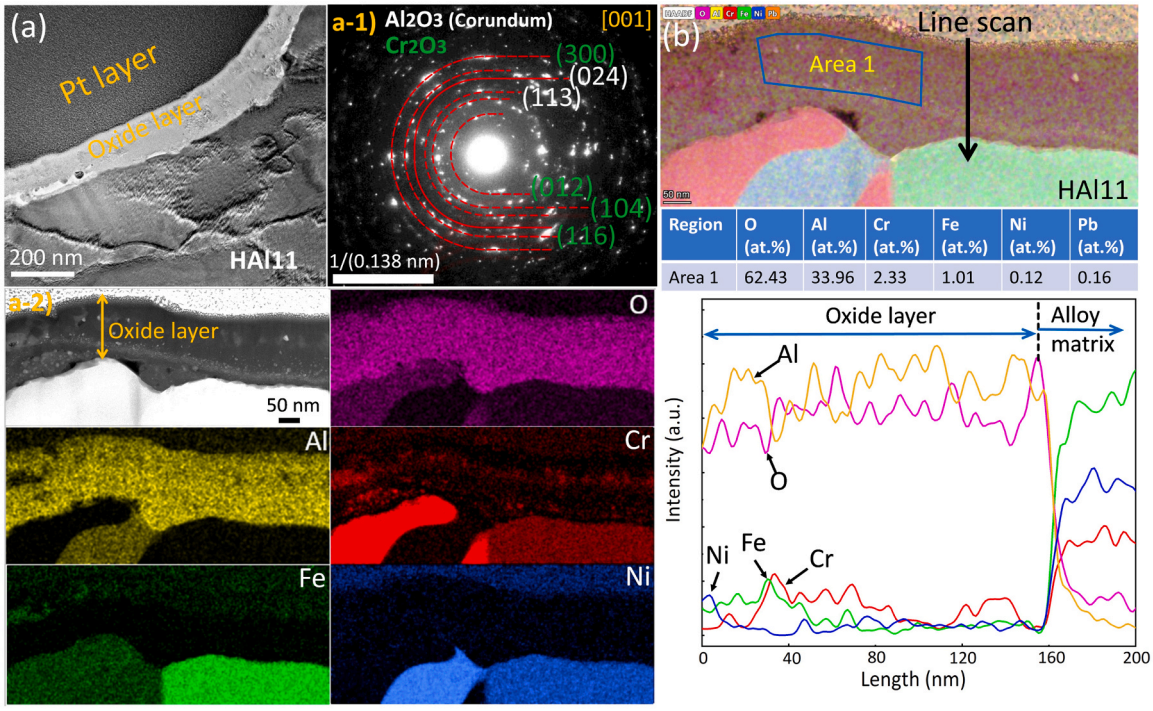

Region	O (at.%)	Al (at.%)	Cr (at.%)	Fe (at.%)	Ni (at.%)	Pb (at.%)
Area 1	62.43	33.96	2.33	1.01	0.12	0.16

Fig. 3. (a) TEM bright-field (BF) image of the oxide layer, (a-1) Selected area electron diffraction (SAED) pattern of the oxide layer, corresponding to corundum Al_2O_3, (a-2) STEM-EDS mapping of the oxide layer; (b) Scanning TEM-EDS regional analysis and line scan across the oxide layer.

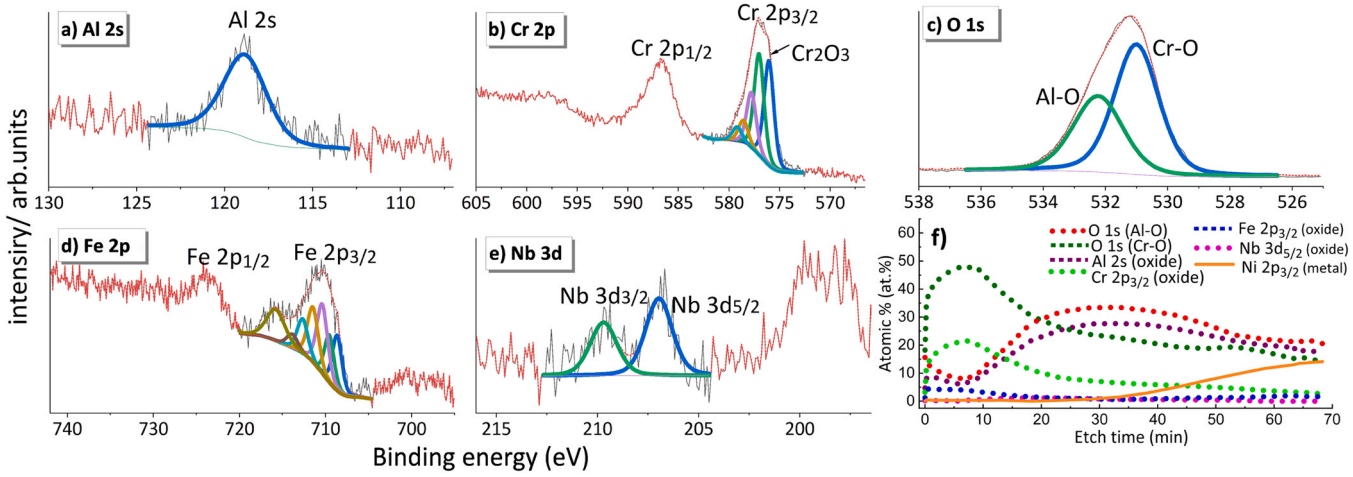

Fig. 4. XPS surface spectra obtained from HAl8^{Nb} after corrosion exposure, (a) Al 2 s, (b) Cr 2p, (c) O 1 s, (d) Fe 2p, (e) Nb 3d, (f) depth profile of elements concentration as a function of sputter time (from 0 to 70 mins).

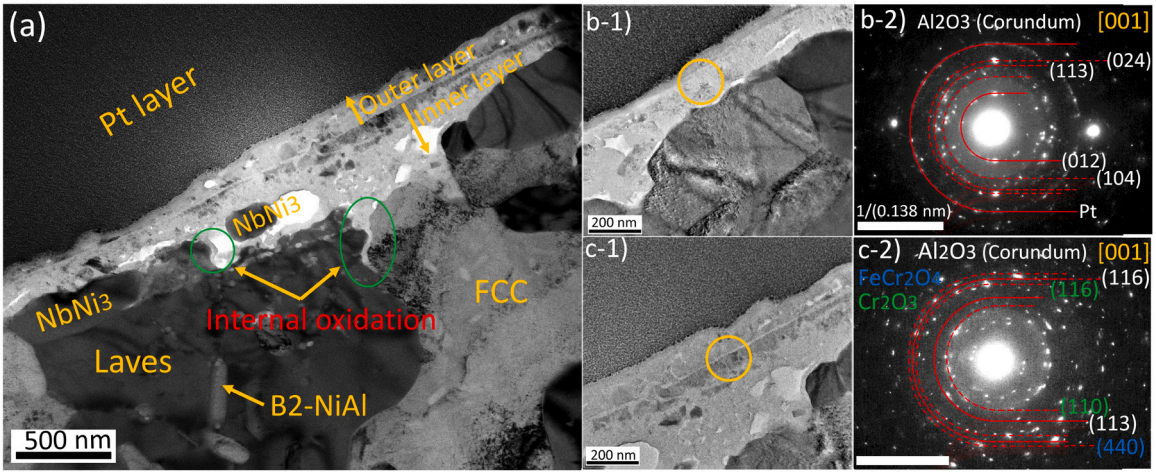

Fig. 5. (a) TEM BF image of the oxide layer passivated on HAl8^{Nb}, (b-1) thin oxide layer region probed by SAED analysis, (b-2) SAED obtained from the circular area in region (b-1), corresponding to corundum Al_2O_3; (c-1) thick oxide layer region probed by SAED analysis; (c-2) SAED obtained from the circular area region (c-1), corresponding to Al_2O_3 (white color), Cr_2O_3 (green color) and $FeCr_2O_4$ (blue color).

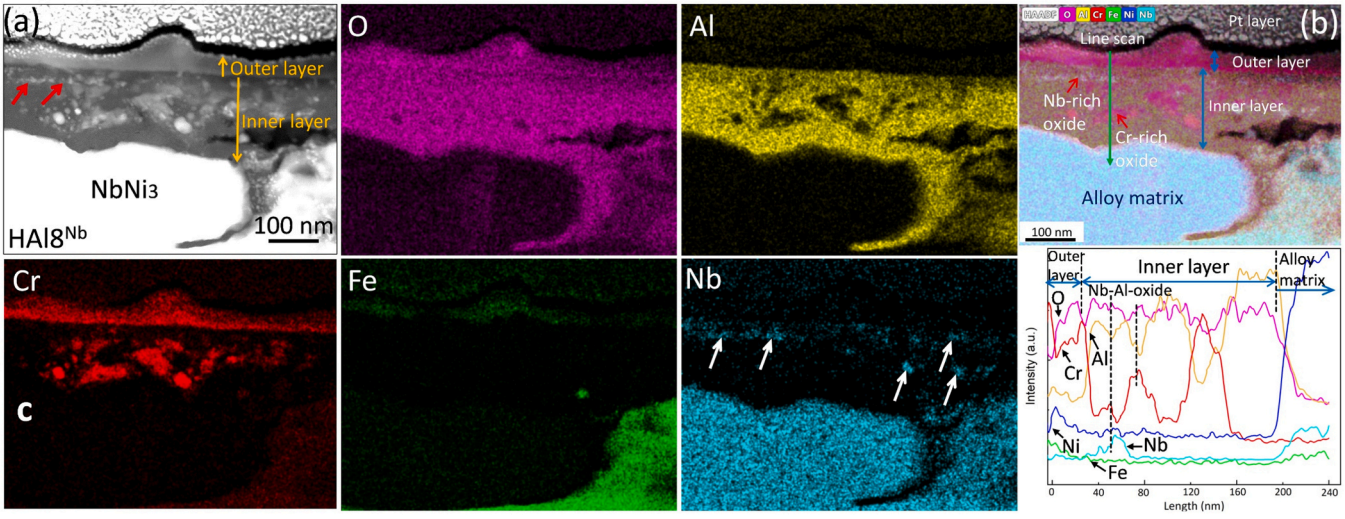

Fig. 6. (a) Scanning TEM BF image and EDS mapping of the oxide layer; (b) HAADF TEM image and EDS line scan across the whole oxide layer region.

cluster in the inner layer corresponds to the bright spots in the original BF image. It is worth noting that Nb shows accumulation in a few spots, closing to the outer/inner layer interface. Due to the controlled oxygen condition, nickel is not considered for oxidation [21]. Another HAADF image and an EDS line scan across the whole oxide layer and the Nb-rich precipitates were performed and shown in Fig. 6b. As further indicated by the EDS line scan, the outermost region contains signals of O, Fe, and Cr. As the scanning depth increases, the signal from Cr, accompanied by the O signal, intensifies and reaches the maximum value at the outer/inner layer interface. The obtained results agree with the formation of Cr_2O_3. The Nb-rich regions marked with red arrows (in Fig. 6b) are related to the bright spots in the BF image (Fig. 6a). Although it is spatially close to the Cr-rich spots, they are separated. Irrespective of a few small peaks related to Nb, the local enrichments of O and Al were also detected when the scan passed through the Nb-rich particles.

We also characterized the oxide layer formed on $HAl8^{Nb}$ at the atomic scale by high-resolution TEM (HR-TEM). Two local regions, Reg-1 and Reg-2, were selected from the outer and the inner layer for the characterization, shown in Fig. 7a. Fig. 7(a-1 Reg-1) shows the atom structure of the outer layer, where a Fast Fourier Transformation (FFT) was applied on the orange frame region. The lattice plane distance identified from this region fits with the value of $FeCr_2O_4$ (space group $Fd\bar{3}m$), namely, the measured lattice plane distance of 0.480 nm corresponds to the {111} plane of $FeCr_2O_4$. The Cr_2O_3 phase underneath the $FeCr_2O_4$ layer was also identified (Supplementary Fig. S8). Another probed region in the inner layer (a-2 Reg-2) confirmed the atomic structure of corundum Al_2O_3, as revealed by the FFT image. The lattice plane distance of 0.351 nm fits with the {012} plane of corundum Al_2O_3.

To further quantify the chemical compositions of the oxide layer, three regional EDS measurements corresponding to the outer, the inner layer, and the Nb-rich region were performed and shown in Fig. 8. In the outer layer (Area 1), the ratio of Cr to Fe is around 3.1 (in at%), which is larger than the stoichiometric number of $FeCr_2O_4$ spinel. This could be due to the formation of the Cr_2O_3 layer in the inner part, as confirmed by the EDS line scan (Fig. 6b). Another measurement of the inner layer (Area 2) indicates that the ratio of O to (Al+Cr) is around 1.54 (in atomic fraction), and the ratio of Al to (Al+Cr) is nearly 0.87, suggesting the presence of $(Al_{0.87}Cr_{0.13})_2O_3$. A local measurement of the Nb-rich precipitates (Area 3) reveals that the ratio of Al:Nb:O is 4.6:1:10.1. The Nb-based oxide could be Nb_2O_5 or $AlNbO_4$ [52]. Considering the local enrichment of Nb and Al in the precipitates (confirmed by EDS line scan in Fig. 6b) and the negative Gibbs free energy (ΔG_f^0) change of the reaction ($Nb_2O_5+Al_2O_3 \rightarrow 2AlNbO_4$, $\Delta G_f^0(650℃) = -1.33$ kJ/mol), a mixture of $AlNbO_4$ and Al_2O_3 was suggested due to a relatively high amount of Al detected. The calculated ratio of Al:Nb:O equals 0.6:1:4.1 after extracting 2 Al_2O_3, approaching the stoichiometric ratio of $AlNbO_4$. Besides, an FFT obtained from the Nb-rich precipitates also fits with $AlNbO_4$ (Supplementary Fig. S9). Considering the above observations, the formation of $AlNbO_4$ was confirmed.

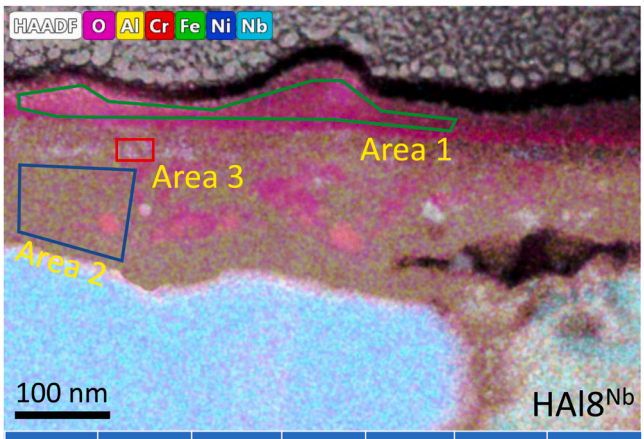

Region	O (at.%)	Al (at.%)	Cr (at.%)	Fe (at.%)	Ni (at.%)	Nb (at.%)
Area 1	71.62	1.98	19.27	6.25	0.31	0.42
Area 2	60.30	33.94	5.09	0.26	0.16	0.24
Area 3	63.92	28.28	0.94	0.26	0.27	6.33

Fig. 8. STEM-EDS regional analysis of the oxide layer; Area 1, Area 2, and Area 3 correspond to the outer layer, the inner layer, and the Nb-rich oxides, respectively.

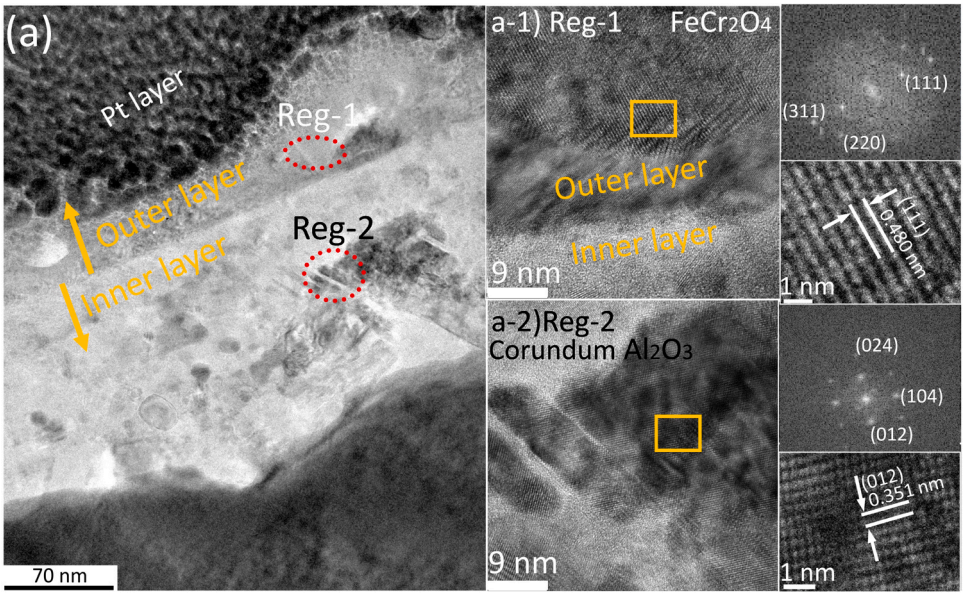

Fig. 7. (a) Bright-field TEM image of oxide scale formed on $HAl8^{Nb}$, (a-1) Reg-1: high-resolution TEM (HR-TEM) image of the oxide layer formed in Reg-1 in (a), atomic scale structure of $FeCr_2O_4$ and Fast Fourier Transformation (FFT) performed at the orange rectangle region in (a-1); (a-2) Reg-2: HR-TEM image of corundum Al_2O_3 formed at Reg-2 in (a), atomic scale structure of oxide layer and FFT performed at the orange rectangle region in (a-2).

4. Discussion

The results presented in the current research attempt to understand the corrosion-oxidation behavior of the three MCAs with varying chemical compositions when exposed to oxygen-containing molten Pb. The sample HAl8 with 7.9 at% Al addition cannot form a protective oxide layer during corrosion exposure. However, both SEM-EDS and XPS depth profiles indicate that the alloy surface region maintains a relatively high Ni content (around 20–25 at%), although the value is lower than the original Ni concentration (36.1 at%). As a comparison, the concentrations of Al and Cr (except for the NiAl-rich precipitates) are much lower after exposure, which might be consumed by oxidation. The XRD measurement (Supplementary Fig. S4) also confirmed the dominance of the FCC phase in the exposed HAl8. All the results revealed that the alloy formed an oxide layer during the exposure. Unfortunately, the oxide layer failed early in the experiment or before sample extraction, and therefore, this alloy is unsuitable for long-term service.

The surface degradation of HAl8 alloy was overcome by introducing two alloy design strategies: increasing the Al content from 7.9 at% to 11.4 at% (HAl11), or adding Nb (5.2 at%, HAl8^{Nb}). Both modified alloys can form and maintain a protective oxide layer without bulk corrosion attack. The type of oxide layer passivated on each alloy was examined by multiple characterization techniques and was summarized in Table 2. In the case of HAl11, the oxide layer chemically consists of two layers: a Fe-, Cr- rich outmost layer and an inner $(Al_{0.94}Cr_{0.06})_2O_3$ layer. The formation of corundum Al_2O_3 (α-Al_2O_3) is possible at such a low temperature since corundum Cr_2O_3 can provide nucleation sites for it [20,53], and the exposure duration is sufficiently long for the transient Al_2O_3 (*i.e.*, θ-Al_2O_3) transforming to the stable α-Al_2O_3. Although oxide nodules (Fe_3O_4) were observed in some regions, no continuous magnetite layer was detected. Such oxide nodules could occur in the early exposure stage when a continuous Al_2O_3 is absent [54]. The oxide layer formed on HAl8^{Nb} is different from that on HAl11, a three-layer composed of an outer layer (an outmost $FeCr_2O_4$ layer plus a Cr_2O_3 layer underneath), an inner $(Al_{0.87}Cr_{0.13})_2O_3$ layer and an IO zone was identified. Unlike the magnetite nodules in HAl11, a continuous Fe-, Cr-rich oxide layer (chromite plus chromia) has formed above the original sample surface of HAl8^{Nb}. The thickness of this layer varies from region to region due to the heterogeneous phase compositions. The inner oxide layer is also based on Al_2O_3-Cr_2O_3 solid solution. However, the ratio of Al to Cr is lower than that of HAl11 due to its low Al content. The interface of the outer and inner layers is located at the original metal surface, which is invisible in HAl11. This evidence reveals their different oxidation processes. For instance, the formation of the chromite and chromia layers is controlled by the outward diffusion of Fe and Cr cations, as observed in the oxidation of CoCrFeNi alloy [55]. Instead, oxygen ingress dominates the inward growth of the Al_2O_3 scale. The invisible interface of HAl11 indicates that the oxidation process is simultaneously determined by the inward oxygen diffusion and the outward diffusion of cations due to a mixture of Cr and Al in the corundum phase (*i.e.*, a mixture of *p*-type and *n*-type oxides). The outward cations diffusion was also confirmed by forming the transitional layer (TL) underneath the oxide layer, where the depletion of Al and Cr was detected. Besides, the formation of the IO zone, which is absent in HAl11, is also due to the extra interfaces between the FCC and the Nb-rich phases, providing a short-circuit diffusion path for oxygen ingress and thus promoting internal Al oxidation [22].

As mentioned in previous work [19], dissolution corrosion (*i.e.*, Ni) and oxidation of alloying elements co-occurred before forming a continuous oxide layer. Whether the corrosion attack occurs depends on several factors, namely, the dissolution rate of alloying elements, the oxide layer growth rate, and the stability of the passivated oxide layer. The alloy with low Al can form a protective oxide layer by adding Nb. According to multiple characterizations of the oxide layer formed on HAl8^{Nb}, four features can be summarized. First, the oxide layer structure is similar everywhere, irrespective of the microstructure in the bulk material (dendrite or inter-dendrite region). Second, the outer layer is based on $FeCr_2O_4$ and Cr_2O_3, and Fe is mainly enriched at the very outermost part (Fig. 6b). The formation of the thin Fe-rich oxide layer provides a first barrier for preventing metallic elements dissolution or penetration of oxidizer. Based on the calculations described in Table 3, adding Nb accelerates the chemical diffusion coefficient of alloying elements in the substrate (HAl8^{Nb} *vs* HAl8), especially Cr and Fe, which is beneficial for the fast building of a continuous Fe-, Cr- rich oxide layer. Third, the inner layer is mainly based on Al_2O_3 doped with a low ratio of Cr_2O_3. The growth of the inner layer occurs at the interface of the alumina layer and the matrix, mainly dominated by the inward O diffusion. Last, $AlNbO_4$ precipitates accumulated at the outer/inner layer interface. By adding Nb, the doping effect (replacing Al cation with Nb cation) and the charge balance promote the mass transport rate (thus the oxide layer thickening rate) [56], as described in Eq. (4). Meanwhile, the precipitation of Nb-rich oxide increases the volume fraction of internal oxides, which are favorable for the rapid establishment of an external oxide scale according to Wagner's model [39].

In addition, we also examined the tensile behaviors of both alloys (HAl11 and HAl8^{Nb}) at elevated temperatures (350 and 500 ℃), and the results are shown in Supplementary Fig. S10 and Table S3. The yield stress (YS) of HAl8^{Nb} is 20.9 % and 27.8 % larger than that of HAl11 at 350 and 500 ℃, respectively. The ultimate tensile stress (UTS) of HAl8^{Nb} is even 45.6 % larger than that of HAl11 at 500 ℃, reaching a value of 809.9 MPa. Interestingly, the YS, UTS, and total elongation (TE) of the HAl8^{Nb} increase as the test temperature increases, which shows a trend opposite to HAl11, whose UTS and TE dramatically decline at 500 ℃, revealing the strong strengthening effect of the Laves phase at high temperature [43]. The fracture surfaces of both samples show dimple

Table 3
Chemical diffusion coefficient (m^2/s) of alloying elements in the bulk alloy at 650 ℃ (referenced to Ni), calculated by Thermo-Calc 2024a (TCNI8 thermodynamic database coupled with MOBNI3 mobility database).

	Al	Cr	Fe	Nb
HAl8	1.9E−18	7.9E−20	8.7E−20	–
HAl11	5.2E−18	1.2E−19	2.0E−19	–
HAl8^{Nb} (in FCC solid solution)	2.4E−18	1.6E−19	1.5E−19	2.4E−19

Table 2
Summary of oxide phases detected in HAl11 and HAl8^{Nb} after corrosion exposure.

	GIXRD	SEM/EDS surface analysis	SEM/EDS cross section analysis	XPS (surface, depth profile)	TEM-SAED	STEM map/line scan	STEM regional scan
HAl11	Fe_3O_4; Cr_2O_3;	ON; Thin oxide layer;	TL layer; No IO;	Al^{3+}; Cr^{3+}; Fe^{2+}; Fe^{3+};	Corundum Al_2O_3; Cr_2O_3;	Mixed oxides: O-, Al-, Cr-rich;	$(Al_{0.94}Cr_{0.06})O_{1.7}$;
HAl8^{Nb}	Fe_3O_4; Cr_2O_3;	Wavy surface morphology; no ON;	IO;	Al^{3+}; Cr^{3+}; Fe^{2+}; Fe^{3+}; Nb^{5+};	Cr_2O_3; Corundum Al_2O_3; $FeCr_2O_4$;	Outer layer: O-, Cr-, Fe-rich; Inner layer: O-, Al-, Cr-rich;	$(Fe, Cr, Al)O_{2.6}$; $(Al_{0.87}Cr_{0.13})O_{1.6}$; $AlNbO_4$;

ON(s): oxide nodule(s); TL: transitional layer; IO: internal oxidation.

morphologies, indicating the ductile characters at elevated temperatures (see Supplementary Fig. S11). Based on these observations, future efforts should be focused on fine-tuning the Nb content to balance the high-temperature corrosion/oxidation resistance and mechanical properties.

$$Al_2O_3 + (Nb \rightarrow Al) \rightarrow Al^{3+} + Nb_{Al} + V'''_{Al} + 3O^x_O \quad (4)$$

Where Nb_{Al} represents the Nb cations in the oxide and $V'''_{Al}$is aluminum vacancy.

Fig. 9a summarizes the thickness of oxide layers formed on various materials, including 9Cr wt% ferritic/martensitic steel, austenitic stainless steel, high entropy alloys/coatings, Max-phase, FeCrAl alloy, and alumina-forming austenitic steels, when exposed to similar oxygen-containing Pb/LBE conditions at varies temperatures up to 3500 hours. Our developed MCAs show excellent corrosion-oxidation resistance in molten Pb and form an ultra-thin oxide scale during exposure. Static thermodynamic calculations were performed by Thermo-calc as shown in Fig. 9(b, c). In the simulation, only inward oxygen ingress was considered. The equilibrium phase present can be predicted as a function of the alloy's oxygen partial pressure (or oxygen content). Here, the melts' equilibrium oxygen partial pressure (P_O) is assumed to be $1.5 * 10^{-22}$ bar (equal to 10^{-6} wt%). According to the calculated plot, HAl8 can only form a chromite layer at such dissolved oxygen conditions. In actual conditions, the oxygen partial pressure at the oxide layer/alloy matrix interface can be significantly reduced once an initial oxide layer forms. Only the oxide with a lower oxygen partial pressure can form, like Al_2O_3. This can explain why Al_2O_3 was observed underneath the Fe- or Cr- rich oxide layer. Increasing Al content introduces two significant changes in the oxide layer formation process, namely, increasing the amount of chromite (*i.e.*, +2.9 %, P_O=10^{-22}) and promoting the formation of Al_2O_3 in a wider oxygen partial pressure range ($< 10^{-23}$ for HAl11 *vs* $< 10^{-24}$ for HAl8). Both processes are beneficial for the rapid establishment of an Al_2O_3 layer. The Nb-containing oxides (*i.e.*, Al(Fe, Nb)O_4) were predicted in $HAl8^{Nb}$, located in between the chromite and Al_2O_3 according to Fig. 9c. This result is also consistent with our experiment results.

Fig. 10 further clarifies the oxide layer formation process of both alloys. Despite the different oxide structures in the investigated alloys, the corrosion-oxidation process can be generally divided into three stages. Initial stage: all the alloying elements are involved in the dissolution and oxidation processes before forming a continuous oxide layer. Transient stage: the alloy surface is covered by a thin oxide scale, where the local chemical composition and oxygen diffusion process are modified. Gradually, selective oxidation like Cr occurs during this stage due to its relatively high activity [57], and forms a continuous oxide layer (*i.e.*, Cr_2O_3 layer for HAl11, and $FeCr_2O_4$ plus Cr_2O_3 layer for $HAl8^{Nb}$). The difference in oxide scale formation between HAl11 and $HAl8^{Nb}$ is mainly attributed to the diffusion process, namely the concurrent diffusion of cations and anions in HAl11. In contrast, the outward diffusion of cations is accelerated in $HAl8^{Nb}$ via Nb doping. Consequently, the outward diffusion of cations is retarded once a continuous oxide layer forms and inner anion (O) penetration dominates the following oxidation process. Steady state: the oxygen partial pressure at the oxide/matrix interface is further reduced. Only the elements with a lower oxygen dissociation partial pressure, such as Nb_2O_5 and Al_2O_3 can be further oxidized. Moreover, the corundum Cr_2O_3 layer also provides nucleation sites for Al_2O_3, resulting in the formation of stable α-Al_2O_3.

5. Conclusion

In summary, the current work aims to understand the improved corrosion-oxidation performances of MCAs when exposed to molten Pb. The results obtained confirm that the alloy design strategies, either increasing the Al concentration to 11.4 at% or adding additional Nb (5.2 at%) and maintaining the current Al and Cr concentrations, are efficient in improving the high-temperature performance of MCAs when exposed to oxygen-containing and corrosive conditions. Both designed alloys can passivate an ultra-thin Al_2O_3-rich oxide scale in liquid Pb. The different oxide layer structures reveal their differences in oxidation mechanism, namely, concurrent diffusion of cations and anions in HAl11 while accelerated outward diffusion of Fe-, Cr- cations for external $FeCr_2O_4/Cr_2O_3$ scale formation in $HAl8^{Nb}$ and inner anion (O) penetration for inner $(Al_{0.87}Cr_{0.13})_2O_3$ layer formation. Adding Nb is beneficial for forming an oxide layer ("Nb-doping effect") via accelerating the bulk diffusion of Cr and Fe, and the precipitation of the Nb-rich oxide increases the volume fraction of internal oxides, further promoting the rapid establishment of an external oxide scale. Besides, adding Nb has additional advantages over only increasing Al content due to the formation of the strengthening Laves phase, which is beneficial for high-temperature mechanical properties.

CRediT authorship contribution statement

Li Yue: Investigation, Methodology, Writing – review & editing. **Müller Georg:** Funding acquisition, Investigation, Project administration, Supervision, Validation, Writing – review & editing. **Gong Xing:** Investigation, Methodology, Writing – review & editing. **Liu Chang:** Investigation, Methodology, Writing – review & editing. **Zhang Xukai:** Investigation, Methodology, Writing – review & editing. **Weisenburger Alfons:** Writing – review & editing, Supervision, Project administration, Funding acquisition, Conceptualization. **Gong Yilun:** Writing – review & editing, Methodology, Investigation. **Ponge Dirk:** Writing – review & editing, Funding acquisition, Project administration, Supervision, Validation. **Shi Hao:** Writing – review & editing, Writing – original draft,

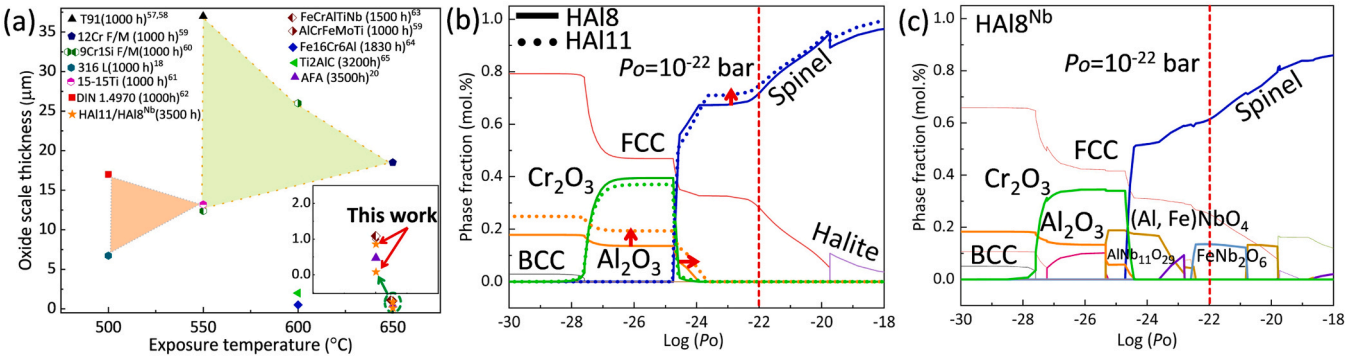

Fig. 9. (a) Comparison of oxide layers formed in our developed MCAs with existing materials after exposed to oxygen-containing Pb/LBE environment; (b) Phase fraction prediction of HAl8 and HAl11 as a function of oxygen partial pressure, calculated by Thermo-calc; (c) Phase fraction prediction of $HAl8^{Nb}$ as a function of oxygen partial pressure, calculated by Thermo-calc.

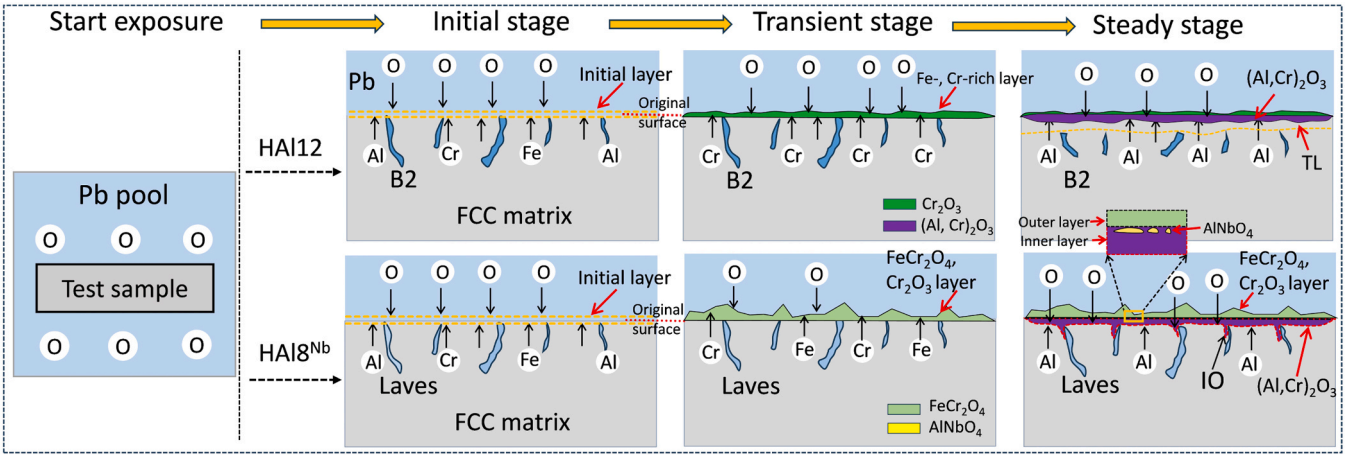

Fig. 10. Schematic diagram describing the evolution of oxide layer formed in the developed MCAs when exposed to oxygen-containing molten Pb condition [58-66].

Methodology, Investigation, Conceptualization. **Azmi Raheleh:** Investigation, Methodology, Writing – review & editing.

Declaration of Competing Interest

The authors declare that they have no known competing financial interests or personal relationships that could have appeared to influence the work reported in this paper.

Acknowledgments

The authors thank Dr. Annette Heinzel (Karlsruhe Institute of Technology) for helping prepare the corrosion tests and Benjamin Breitbach (Max Planck Institute for Sustainable Materials) for assistance with GIXRD measurement.

Appendix A. Supporting information

Supplementary data associated with this article can be found in the online version at doi:10.1016/j.corsci.2025.112990.

Data availability

Data will be made available on request.

References

[1] S. Eswarappa Prameela, T.M. Pollock, D. Raabe, M.A. Meyers, A. Aitkaliyeva, K. L. Chintersingh, Z.C. Cordero, L. Graham-Brady, Materials for extreme environments, Nat. Rev. Mater. 8 (2023) 81–88.
[2] V.H. Dalvi, S.V. Panse, J.B. Joshi, Solar thermal technologies as a bridge from fossil fuels to renewables, Nat. Clim. Change 5 (2015) 1007–1013.
[3] R. Pitz-Paal, Concentrating solar power: still small but learning fast, Nat. Energy 2 (2017) 1–2.
[4] H. Kim, D.A. Boysen, J.M. Newhouse, B.L. Spatocco, B. Chung, P.J. Burke, D. J. Bradwell, K. Jiang, A.A. Tomaszowska, K. Wang, Liquid metal batteries: past, present, and future, Chem. Rev. 113 (2013) 2075–2099.
[5] K. Wang, K. Jiang, B. Chung, T. Ouchi, P.J. Burke, D.A. Boysen, D.J. Bradwell, H. Kim, U. Muecke, D.R. Sadoway, Lithium–antimony–lead liquid metal battery for grid-level energy storage, Nature 514 (2014) 348–350.
[6] A.M. Amin, E. Croiset, W. Epling, Review of methane catalytic cracking for hydrogen production, Int. J. Hydrog. Energy 36 (2011) 2904–2935.
[7] G. Shu, J. Wang, B. Liu, J. Tian, Z. Liu, Solar driven methane cracking to produce hydrogen and carbon: a review, Int. J. Hydrog. Energy 72 (2024) 485–497.
[8] M. Mathew, Nuclear energy: a pathway towards mitigation of global warming, Prog. Nucl. Energy 143 (2022) 104080.
[9] A.Z. Paydar, S.K.M. Balgehshiri, B. Zohuri, Advanced reactor concepts (ARC): a new nuclear power plant perspective producing energy, Elsevier, 2023.
[10] R. Betti, A milestone in fusion research is reached, Nat. Rev. Phys. 5 (2023) 6–8.
[11] C. Amy, D. Budenstein, M. Bagepalli, D. England, F. DeAngelis, G. Wilk, C. Jarrett, C. Kelsall, J. Hirschey, H. Wen, Pumping liquid metal at high temperatures up to 1,673 kelvin, Nature 550 (2017) 199–203.
[12] B.A. Pint, J. Jun, M. Romedenne, Compatibility of SiC with ODS FeCrAl in flowing Pb-Li at 600°–700°C, Fusion Eng. Des. 166 (2021) 112389.
[13] Y. Wang, A.P. Olson, C. Falconer, B. Kelleher, I. Mitchell, H. Zhang, K. Sridharan, J. W. Engle, A. Couet, Radionuclide tracing based in situ corrosion and mass transport monitoring of 316L stainless steel in a molten salt closed loop, Nat. Commun. 15 (2024) 3106.
[14] E. González-Roubaud, D. Pérez-Osorio, C. Prieto, Review of commercial thermal energy storage in concentrated solar power plants: steam vs. molten salts, Renew. Sustain. Energy Rev. 80 (2017) 133–148.
[15] Y. Ahn, S.J. Bae, M. Kim, S.K. Cho, S. Baik, J.I. Lee, J.E. Cha, Review of supercritical CO_2 power cycle technology and current status of research and development, Nuc. Eng. Technol. 47 (2015) 647–661.
[16] E. González-Roubaud, D. Pérez-Osorio, C. Prieto, Handbook on lead-bismuth eutectic alloy and lead properties, materials compatibility, thermal-hydraulics and technologies-2015 edition (No. NEA–7268), Organisation for Economic Co-Operation and Development, 2015.
[17] X. Gong, M.P. Short, T. Auger, E. Charalampopoulou, K. Lambrinou, Environmental degradation of structural materials in liquid lead-and lead-bismuth eutectic-cooled reactors, Prog. Mater. Sci. 126 (2022) 100920.
[18] K. Lambrinou, E. Charalampopoulou, T. Van der Donck, R. Delville, D. Schryvers, Dissolution corrosion of 316L austenitic stainless steels in contact with static liquid lead-bismuth eutectic (LBE) at 500 °C, J. Nucl. Mater. 490 (2017) 9–27.
[19] J. Zhang, N. Li, Analysis on liquid metal corrosion–oxidation interactions, Corros. Sci. 49 (2007) 4154–4184.
[20] H. Shi, R. Fetzer, C. Tang, D.V. Szabó, S. Schlabach, A. Heinzel, A. Weisenburger, A. Jianu, G. Müller, The influence of Y and Nb addition on the corrosion resistance of Fe-Cr-Al-Ni model alloys exposed to oxygen-containing molten Pb, Corros. Sci. 179 (2021) 109152.
[21] G. Müller, A. Heinzel, G. Schumacher, A. Weisenburger, Control of oxygen concentration in liquid lead and lead–bismuth, J. Nucl. Mater. 321 (2003) 256–262.
[22] K. Messaoudi, A. Huntz, B. Lesage, Diffusion and growth mechanism of Al_2O_3 scales on ferritic Fe-Cr-Al alloys, Mater. Sci. Eng. A. 247 (1998) 248–262.
[23] J. Ejenstam, M. Halvarsson, J. Weidow, B. Jönsson, P. Szakalos, Oxidation studies of Fe10CrAl-RE alloys exposed to Pb at 550 °C for 10,000h, J. Nucl. Mater. 443 (2013) 161–170.
[24] M.P. Short, R.G. Ballinger, A functionally graded composite for service in high-temperature lead-and lead-bismuth–cooled nuclear reactors—I: design, Nucl. Technol. 177 (2012) 366–381.
[25] J. Zhang, A review of steel corrosion by liquid lead and lead–bismuth, Corros. Sci. 51 (2009) 1207–1227.
[26] J.W. Yeh, S.K. Chen, S.J. Lin, J.Y. Gan, T.S. Chin, T.T. Shun, C.H. Tsau, S.Y. Chang, Nanostructured high-entropy alloys with multiple principal elements: novel alloy design concepts and outcomes, Adv. Eng. Mater. 6 (2004) 299–303.
[27] D.B. Miracle, O.N. Senkov, A critical review of high entropy alloys and related concepts, Acta Mater. 122 (2017) 448–511.
[28] O.El Atwani, H.T. Vo, M.A. Tunes, C. Lee, A. Alvarado, N. Krienke, J.D. Poplawsky, A.A. Kohnert, J. Gigax, W.Y. Chen, A quinary WTaCrVHf nanocrystalline refractory high-entropy alloy withholding extreme irradiation environments, Nat. Commun. 14 (2023) 2516.
[29] M. Li, H. Sun, X. Tan, H. Zhang, J. Liu, A novel entropy-stabilized oxide coating thermally grown from a valve metal-based complex concentrated alloy, Mater. Today 74 (2024) 46.
[30] L. Han, F. Maccari, I. Soldatov, N.J. Peter, I.R. Souza Filho, R. Schäfer, O. Gutfleisch, Z. Li, D. Raabe, Strong and ductile high temperature soft magnets through Widmanstätten recipitates, Nat. Commun. 14 (2023) 8176.
[31] Y.J. Liang, L. Wang, Y. Wen, B. Cheng, Q. Wu, T. Cao, Q. Xiao, Y. Xue, G. Sha, Y. Wang, High-content ductile coherent nanoprecipitates achieve ultrastrong high-entropy alloys, Nat. Commun. 9 (2018) 4063.

[32] N.T.C. Nguyen, P. Asghari-Rad, P. Sathiyamoorthi, A. Zargaran, C.S. Lee, H.S. Kim, Ultrahigh high-strain-rate superplasticity in a nanostructured high-entropy alloy, Nat. Commun. 11 (2020) 2736.
[33] T. Yang, Y. Zhao, W. Li, C. Yu, J. Luan, D. Lin, L. Fan, Z. Jiao, W. Liu, X. Liu, Ultrahigh-strength and ductile superlattice alloys with nanoscale disordered interfaces, Science 369 (2020) 427–432.
[34] Y. Yamamoto, M.P. Brady, M.L. Santella, H. Bei, P.J. Maziasz, B.A. Pint, Overview of strategies for high-temperature creep and oxidation resistance of alumina-forming austenitic stainless steels, Metall. Mater.. Trans. A 42 (2011) 922–931.
[35] H. Shi, Alumina Forming Alloys (steels, High Entropy Materials) for the Mitigation of Compatibility Issues With Liquid Metals and Steam in Energy Related. High-temperature Applications, Karlsruher Institut für Technologie (KIT), Karlsruhe, 2020.
[36] H. Shi, A. Jianu, R. Fetzer, D.V. Szabo, S. Schlabach, A. Weisenburger, C.C. Tang, A. Heinzel, F. Lang, G. Mueller, Compatibility and microstructure evolution of Al-Cr-Fe-Ni high entropy model alloys exposed to oxygen-containing molten lead, Corros. Sci. 189 (2021) 109593.
[37] F. Stott, G. Wood, J. Stringer, The influence of alloying elements on the development and maintenance of protective scales, Oxid. Met. 44 (1995) 113–145.
[38] C. Tedmon, The effect of oxide volatilization on the oxidation kinetics of Cr and Fe-Cr alloys, J. Electrochem. Soc. 113 (1966) 766.
[39] C. Wagner, Reaktionstypen bei der Oxydation von Legierungen, Z. -fuer-Elektrochem. 63 (1959) 772.
[40] R.A. Rapp, The transition from internal to external oxidation and the formation of interruption bands in silver-indium alloys, Acta Metall. 9 (1961) 730–741.
[41] P. Kofstad, C. Steidel, High temperature oxidation of metals, J. Electrochem. Soc. 114 (1967) 167C.
[42] Y. Yamamoto, M.P. Brady, Z.P. Lu, P.J. Maziasz, C.T. Liu, B.A. Pint, K.L. More, H. Meyer, E.A. Payzant, Creep-resistant, Al_2O_3-forming austenitic stainless steels, Science 316 (2007) 433–436.
[43] A. Thomas, M. El-Wahabi, J. Cabrera, J. Prado, High temperature deformation of Inconel 718, J. Mater. Process. Technol. 177 (2006) 469–472.
[44] X. Huang, X. Gong, M. Song, J. Chen, F. Hu, Y. Yin, J. Xiao, H. Wang, H. Wang, H. Gong, Liquid metal embrittlement susceptibility of a high-entropy alloy exposed to oxygen-depleted liquid lead-bismuth eutectic at 250 and 350 °C, J. Nucl. Mater. 528 (2020) 151859.
[45] K.L. Parry, A. Shard, R. Short, R. White, J. Whittle, ARXPS characterisation of plasma polymerised surface chemical gradients, Surf. Interface Anal. 38 (2006) 1497–1504.
[46] J. Scofield, Hartree-Slater subshell photoionization cross-sections at 1254 and 1487 eV, J. Electron Spectrosc. Relat. P8 (1976) 129–137.
[47] S. Tanuma, C. Powell, D. Penn, Calculations of electron inelastic mean free paths. IX. Data for 41 elemental solids over the 50 eV to 30 keV range, Surf. Interface Anal. 43 (2011) 689–713.
[48] M. Birkholz, Thin Film Analysis by X-ray Scattering, John Wiley & Sons, 2006.
[49] I. Olefjord, H. Mathieu, P. Marcus, Intercomparison of surface analysis of thin aluminum oxide films, Surf. Interface Anal. 15 (1990) 681–692.
[50] P. Zhao, H. Zhao, J. Yu, H. Zhang, H. Gao, Q. Chen, Crystal structure and properties of Al_2O_3-Cr_2O_3 solid solutions with different Cr_2O_3 contents, Ceram. Int. 44 (2018) 1356–1361.
[51] J.F. Moulder, W.F. Stickle, P.E. Sobol, K.D. Bomben, Handbook of X-ray photoelectron spectroscopy, Perkin-Elmer, USA, 1992.
[52] S. Liu, W. Kai, J. Hou, Y. Zhao, Q. Li, C.-h Yang, T. Yang, J.J. Kai, Oxidation behaviors and mechanical properties of $L1_2$-strengthened high-entropy alloys at 700 ℃, Corros. Sci. 206 (2022) 110499.
[53] S. Yoneda, S. Hayashi, I. Saeki, S. Ukai, The effect of Cr on the lifetime of Al-rich amorphous oxide layer formed on Fe–Cr–Al alloys at 650 °C, Oxid. Met. 88 (2017) 669–686.
[54] P. Tomaszewicz, G. Wallwork, The oxidation of high-purity iron-chromium-aluminum alloys at 800 °C, Oxid. Met. 20 (1983) 75–109.
[55] X.X. Yu, M.A. Taylor, J.H. Perepezko, L.D. Marks, Competition between thermodynamics, kinetics and growth mode in the early-stage oxidation of an equimolar CoCrFeNi alloy, Acta Mater. 196 (2020) 651–659.
[56] A. Vayyala, I. Povstugar, T. Galiullin, D. Naumenko, W. Quadakkers, H. Hattendorf, J. Mayer, Effect of Nb addition on oxidation mechanisms of high Cr ferritic steel in Ar–H_2–H_2O, Oxid. Met. 92 (2019) 471–491.
[57] D.J. Young, High temperature oxidation and corrosion of metals, Elsevier, 2008.
[58] L. Martinelli, F. Balbaud-Célérier, A. Terlain, S. Delpech, G. Santarini, J. Favergeon, G. Moulin, M. Tabarant, G. Picard, Oxidation mechanism of a Fe–9Cr–1Mo steel by liquid Pb–Bi eutectic alloy (Part I), Corros. Sci. 50 (2008) 2523–2536.
[59] L. Martinelli, F. Balbaud-Célérier, Modelling of the oxide scale formation on Fe-Cr steel during exposure in liquid lead-bismuth eutectic in the 450–600 °C temperature range, Mater. Corros.. 62 (2011) 531–542.
[60] J. Yang, K. Shi, W. Zhang, Q. Chen, Z. Ning, C. Zhu, J. Liao, Y. Yang, N. Liu, J. Yang, A novel AlCrFeMoTi high-entropy alloy coating with a high corrosion-resistance in lead-bismuth eutectic alloy, Corros. Sci. 187 (2021) 109524.
[61] H. Shi, H. Wang, R. Fetzer, A. Heinzel, A. Weisenburger, K. Wang, A. Jianu, G. Müller, Influence of Si addition on the corrosion behavior of 9 wt% Cr ferritic/martensitic steels exposed to oxygen-controlled molten Pb-Bi eutectic at 550 and 600 °C, Corros. Sci. 193 (2021) 109871.
[62] A. Heinzel, A. Weisenburger, G. Müller, Corrosion behavior of austenitic steels in liquid lead bismuth containing 10^{-6} wt% and 10^{-8} wt% oxygen at 400–500 °C, J. Nucl. Mater. 448 (2014) 163–171.
[63] E. Charalampopoulou, R. Delville, M. Verwerft, K. Lambrinou, D. Schryvers, Transmission electron microscopy study of complex oxide scales on DIN 1.4970 steel exposed to liquid Pb-Bi eutectic, Corros. Sci. 147 (2019) 22–31.
[64] J. Yang, J. Liang, G. Wang, J. Liao, S. Qiu, W. Zhang, J. Yang, Microstructure, mechanical properties and lead-bismuth eutectic corrosion behavior of FeCrAlTiNb high-entropy alloy coatings, Corros. Sci. 222 (2023) 111407.
[65] A. Jianu, R. Fetzer, A. Weisenburger, S. Doyle, M. Bruns, A. Heinzel, P. Hosemann, G. Mueller, Stability domain of alumina thermally grown on Fe–Cr–Al-based model alloys and modified surface layers exposed to oxygen-containing molten Pb, J. Nucl. Mater. 470 (2016) 68–75.
[66] H. Shi, R. Azmi, L. Han, C. Tang, A. Weisenburger, A. Heinzel, J. Maibach, M. Stüber, K. Wang, G. Müller, Corrosion behavior of Al-containing MAX-phase coatings exposed to oxygen containing molten Pb at 600 °C, Corros. Sci. 201 (2022) 110275.